The Dynamics of Southern Ocean Storm Tracks

Christopher C. Chapman*

Research School of Earth Sciences, and ARC Centre of Excellence for Climate System Science, The Australian National University, Canberra, Australian Capital Territory, and CSIRO Wealth From Oceans Flagship, Hobart, Tasmania, Australia

Andrew McC. Hogg

Research School of Earth Sciences, and ARC Centre of Excellence for Climate System Science, The Australian National University, Canberra, Australian Capital Territory, Australia

Andrew E. Kiss

School of Physical, Mathematical and Environmental Sciences, University of New South Wales Canberra at the Australian Defence Force Academy, Australia, and ARC Centre of Excellence for Climate System Science, The Australian National University, Canberra, Australian Capital Territory, Australia

Stephen R. Rintoul

CSIRO Wealth from Oceans Flagship, and Antarctic Climate and Ecosystems Cooperative Research Centre, University of Tasmania, Hobart, Tasmania, Australia

ABSTRACT

The mechanisms that initiate and maintain oceanic ''storm tracks'' (regions of anomalously high eddy kinetic energy) are studied in a wind-driven, isopycnal, primitive equation model with idealized bottom topography. Storm tracks are found downstream of the topography in regions strongly influenced by a large-scale stationary meander that is generated by the interaction between the background mean flow and the topography. In oceanic storm tracks the length scale of the stationary meander differs from that of the transient eddies, a point of distinction from the atmospheric storm tracks. When the zonal length and height of the topography are varied, the storm-track intensity is largely unchanged and the downstream storm-track length varies only weakly. The dynamics of the storm track in this idealized configuration are investigated using a wave activity flux (related to the Eliassen–Palm flux and eddy energy budgets). It is found that vertical fluxes of wave activity (which correspond to eddy growth by baroclinic conversion) are localized to the region influenced by the standing meander. Farther downstream, organized horizontal wave activity fluxes (which indicate eddy energy fluxes) are found. A mechanism for the development of oceanic storm tracks is proposed: the standing meander initiates localized conversion of energy from the mean field to the eddy field, while the storm track develops downstream of the initial baroclinic growth through the ageostrophic flux of Montgomery potential. Finally, the implications of this analysis for the parameterization and prediction of storm tracks in ocean models are discussed.

* Current affliation: CNRS/LOCEAN-IPSL, Université de Pierre et Marie Curie, Paris, France.

Corresponding author address: C. C. Chapman, CNRS/LOCEAN-IPSL, Université de Pierre et Marie Curie, Paris, 75252 Cedex 05, France.
E-mail: chris.chapman.28@gmail.com

1. Introduction

Storm tracks, regions of localized, enhanced eddy kinetic energy (EKE), are a long known and well-studied feature of the midlatitude atmosphere (Blackmon 1976; Chang et al. 2002). In atmospheric storm tracks, strong anomalous vortices preferentially form and grow by the baroclinic instability process (Hoskins and Valdes 1990)
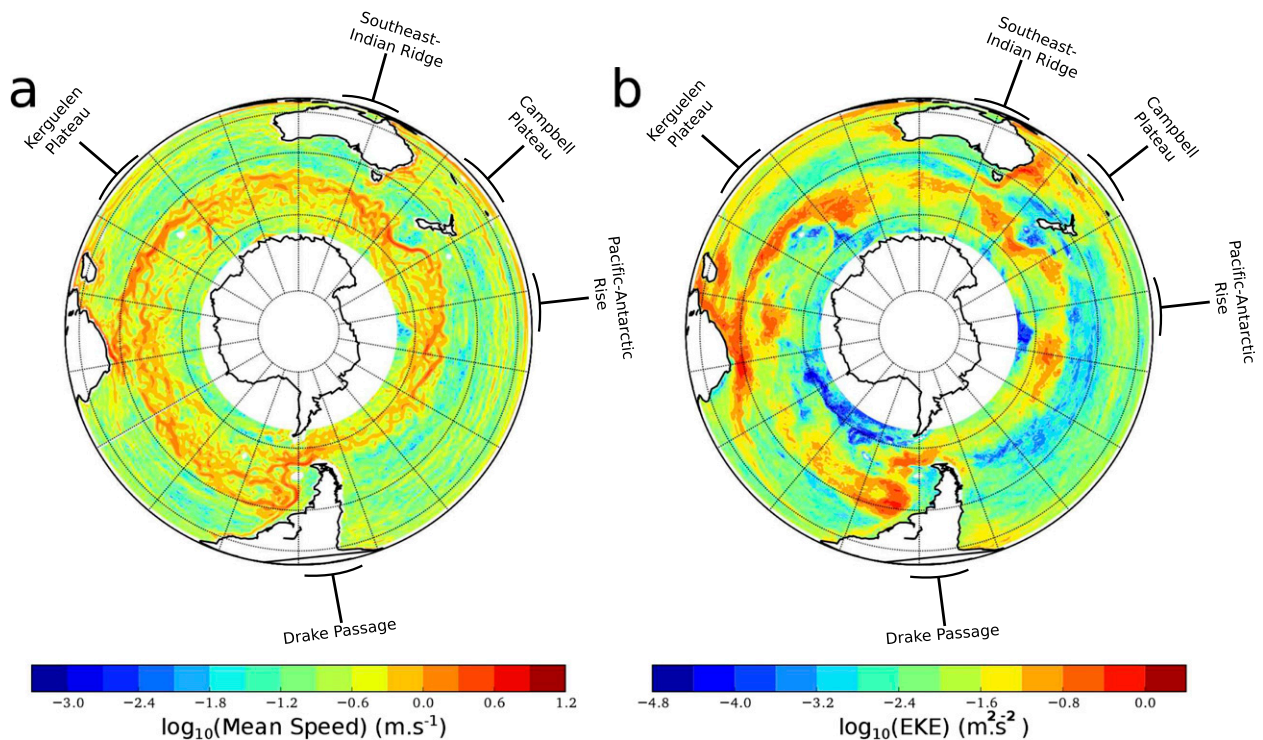
FIG. 1. The 5-yr time-mean (a) current speed and (b) transient EKE in the Southern Ocean calculated from output of the OFES model. Note the logarithmic color scale. The approximate longitude of large topographic features is labeled.

and decay downstream of their genesis regions with characteristic time scales known as the "baroclinic life-cycle" (Lindzen and Farrell 1980). Storm tracks are found near the cores of the midlatitude jet streams (Blackmon 1976) but show zonal asymmetry. In the Northern Hemisphere, there are two distinct storm tracks: one over the North Pacific basin, another over the North Atlantic basin (Hoskins and Hodges 2002). The storm tracks in the Southern Hemisphere are found primarily over the South Atlantic and Indian Ocean basins, although the zonal asymmetry of the EKE fields is not as strong as that of the Northern Hemisphere (Hoskins and Hodges 2005).

As improvements in observations and numerical models have enabled the regional variations in the Southern Ocean's eddy field to be explored, it has become clear that the strength of the eddy field is not homogenous but is concentrated in particular regions, sometimes referred to as eddy or mixing "hot spots" (Morrow et al. 1994; Hughes and Ash 2001; Hughes 2005; Morrow et al. 2010; Naveira Garabato et al. 2011; Venaille et al. 2011; Thompson and Sallée 2012; Chapman 2014). Several recent studies have argued that these hot spots may be similar to atmospheric storm tracks (Williams et al. 2007, hereinafter WWH07; Thompson and Naveira Garabato 2014; Bischoff and Thompson 2014). The connection between atmospheric

storm tracks and regions of enhanced EKE in the ocean was first made explicit by WWH07, who applied a temporal high-pass filter to altimetry-derived sea surface height fields to produce maps of the EKE in the Southern Ocean. Areas of high EKE were noted in the southwest Indian Ocean (particularly in the region coincident with the passage of Agulhas rings), south of New Zealand where flow is steered by the Campbell Plateau, westward of the Pacific–Antarctic Rise, and through Drake Passage.

As motivation for this study, we present a similar analysis to WWH07 in Fig. 1, using 5 yr of velocity field output of the eddy-resolving Ocean General Circulation Model for the Earth Simulator (OFES) of Masumoto et al. (2004), temporally high-pass filtered to produce a time-averaged map of EKE density, as in WWH07. Regions of high EKE density likened to storm tracks by WWH07 can be seen in Fig. 1b, as well as downstream of the Kerguelen Plateau region. Almost all storm-track regions away from western boundary currents are found downstream of large topographic features (labeled) (Thompson and Sallée 2012).

The purpose of this study is to explore the dynamics of storm tracks in the Southern Ocean and to develop a physical mechanism that explains their formation near large topographic features and the extension of high EKE farther downstream.

a. A review of the dynamics of atmospheric storm tracks

The persistence of high EKE in certain geographical regions presented a quandary to meteorologists studying the phenomenon: if the storm tracks are formed by baroclinic instability, and baroclinic eddies act to reduce the background meridional temperature gradient, how can storm tracks regionally persist? Additionally, the maximum EKE is often found downstream of the most baroclinically unstable regions. Numerous studies have sought to describe the influence of external forcing on storm-track structure. Storm tracks are known to be influenced by thermal forcing caused by the land/ocean temperature contrast at continental boundaries (Hoskins and Valdes 1990; Wilson et al. 2009; Kaspi and Schneider 2011), by orographically induced stationary waves (Simmons and Hoskins 1979; Lee and Mak 1996; Kaspi and Schneider 2013), and by the background flow (Hartmann 1983; Son et al. 2009). The relative importance of each individual forcing is still a matter of debate (Chang et al. 2002).

The fact that atmospheric storm tracks form downstream of regions with strong local surface forcing gives some hints to their dynamical origins. Topography and surface heating are known to strongly influence the position and orientation of jets (Held 1983) and destabilize the flow when subject to small-amplitude perturbations (Robinson and McWilliams 1974; Pedlosky 1987, section 7.13). Surface forcing can also lead to the development of stationary and resonant Rossby waves (Held 1983). Large-scale stationary waves have been shown to significantly influence the initiation of atmospheric storm tracks and their zonal extent (Kaspi and Schneider 2013).

The propagation or advection of individual eddies cannot explain the zonal extent of atmospheric storm tracks or the appearance of growing baroclinic disturbances in regions with low baroclinicity (Orlanski and Chang 1993; Chang and Orlanski 1993). Two studies provide an explanation. The first (Simmons and Hoskins 1979) showed, using an idealized primitive equation model and a set of simplified, quasi-analytic calculations, that baroclinic eddies could develop downstream of a localized finite-amplitude perturbation independent of the propagation of the initial disturbance (so-called downstream development). There were significant differences between the downstream development excited by a finite-amplitude perturbation and those that grow from unstable small-amplitude perturbations. For example, the growth rate of the finite-amplitude downstream eddies was about twice that of the fastest-growing mode computed from a linear stability analysis. The second study (Chang and Orlanski 1993) used a primitive equation model with an idealized configuration to show that the downstream development of Simmons

and Hoskins (1979) occurs through the dispersion of eddy energy downstream because of the ageostrophic pressure flux (explained further in section 3). Decaying eddies emit energy that propagates downstream at the approximate Rossby wave group velocity and can be used by other eddies to grow, even in regions of low baroclinicity. Energy is passed from one eddy to another in the downstream development process. Danielson et al. (2006) presented an example of this effect in an analysis of cyclone development over the North Pacific using atmospheric reanalysis data. A single wave packet emanating from the Asian mainland caused two cyclones to develop as it propagated across the ocean.

Taken together, Simmons and Hoskins (1979) and Chang and Orlanski (1993) provide a compelling physical mechanism for the formation and persistence of atmospheric storm tracks. Large-scale forcing provides a localized environment for the development of baroclinic disturbances. The initial disturbance propagates downstream and emits eddy energy as it decays, which can cause further baroclinic development downstream of the initial forcing region.

b. Storm tracks in the Southern Ocean

WWH07 found that the oceanic EKE hotspots shared several similarities with atmospheric tracks: baroclinically unstable regions were found upstream of the maximum EKE, and the eddy forcing had a similar overall impact on the mean jets. However, WWH07 noted several differences between atmospheric and oceanic storm tracks. Specifically, the length scale of the transient eddies relative to the large-scale forcing (discussed below) and the fact that the time-mean flow in the Southern Ocean is not always zonal. Additionally, the transient eddies in atmospheric storm tracks are mobile (Danielson et al. 2006), moving as a coherent vortex in an eastward direction while growing and decaying. However, in the Southern Ocean, many high EKE regions do not show coherent eddy propagation (Venaille et al. 2011), and phase speeds are very small and sometimes negative (Chelton et al. 2011; Klocker and Abernathey 2014).

Until recently, most studies have focused on the large-scale distribution of EKE (e.g., Meredith and Hogg 2006). However, some recent work has focused on the observed inhomogeneity of the Southern Ocean's eddy field. Venaille et al. (2011) investigated the hypothesis that the controlling mechanism of mesoscale eddies is baroclinic instability acting locally on the mean state, finding that neither the magnitude nor the dominant length scales of the eddy field could be explained by local factors alone. They concluded that the eddy field is, at least partially, set by nonlocal effects, such as eddies or energy propagating into a region from afar. This result is supported by

O'Kane et al. (2014), who demonstrated in an eddy permitting GCM that baroclinic disturbances generated in the subtropics were able to propagate and influence the eddy field long distances from their genesis regions.

In an analysis of an eddy-resolving GCM, Thompson and Naveira Garabato (2014) found that regions with high transient eddy activity were located downstream of significant standing meanders, which form where the mean flow is steered by submarine topography (Hughes 2005; Sokolov and Rintoul 2007). Bischoff and Thompson (2014) used a primitive equation model with idealized topography (an isolated bump) to investigate how topography can act to localize EKE. Their results showed that a single, strong jet, forced to deviate from a zonal path by topography, forms both a standing meander and a high EKE region downstream of the hill, reminiscent of Southern Ocean storm tracks described by WWH07. The elevated EKE field extends far downstream of the meander and the associated baroclinically unstable region. In a similar arrangement to atmospheric storm tracks, Bischoff and Thompson (2014) show that the standing meander induces a region of elevated baroclinic instability, attributable to increases in the isopycnal slope, localized upstream of the peak EKE. Similar work by Abernathey and Cessi (2014) compared the local cross-stream heat transport in an ocean model with and without a meridionally oriented topographic ridge. They found that the standing meander due to the ridge acted to concentrate the eddy activity and meridional heat flux downstream of the ridge, while in the flat-bottomed experiment, eddy activity was homogeneously distributed throughout the domain. The mechanism controlling the downstream extension of the EKE field was not addressed in either study.

Oceanic storm tracks may be important for ocean dynamics, as regions of high EKE can significantly accelerate or decelerate the mean jets by Reynolds stress divergence (Hughes and Ash 2001; WWH07). Storm tracks may also influence the cross-stream exchange of tracers. Sallée et al. (2008), using simulated Lagrangian drifters applied to surface velocity fields derived from satellite altimetry, found a correlation between EKE and cross-stream eddy diffusivity κ that was strong enough to suggest a simple parameterization of κ by EKE. Thompson and Sallée (2012) showed both in a quasigeostrophic (QG) channel model of the Southern Ocean with idealized topography and in flow fields derived from satellite altimetry that regions of enhanced EKE were correlated with regions that more readily permit Lagrangian particles to cross-latitude lines, although they emphasize that aspects of the mean flow are also important in setting the meridional transport. However, other studies that have attempted to elucidate the precise relationship between EKE hotspots and eddy diffusivity have shown that, by itself, EKE may not be a good indicator of strong mixing regions (Jayne and Marotzke 2002; Shuckburgh et al. 2009).

c. Goals of this study

In this study, we investigate the role of topographically generated stationary waves in setting the shape and intensity of oceanic storm tracks. We propose a mechanism, based on those used to describe atmospheric storm tracks, to explain the initiation and downstream extension of oceanic storm tracks. Our work can be seen as an extension of the recent work of Abernathey and Cessi (2014) and Bischoff and Thompson (2014), as we are concerned with the zonal, downstream persistence of the elevated EKE outside of the baroclinically unstable regions, as well as the initiation of the storm track. We also examine the sensitivity and zonal extent of the storm track to changes in the shape of the topography.

Oceanic parameter regimes differ significantly from those of the atmosphere, and it is unclear whether the atmospheric models can be applied to oceanic storm tracks. Transient "synoptic" eddies in the atmosphere have length scales ~1000 km in the midlatitudes (Barnes and Hartmann 2012), which are similar to the length scale of forced, stationary waves (Held 1983). The variability of the Southern Ocean is generally associated with two dynamical phenomena: mesoscale eddies, which are governed by nonlinear dynamics, and Rossby waves, which are primarily linear. Mesoscale eddies have short length scales, generally $\sim 2\pi R_{d_1}$, where R_{d_1} is the first baroclinic Rossby deformation radius, generally 10–30 km (Chelton et al. 1998) in the Southern Ocean. Linear Rossby waves are a larger-scale phenomenon, with wavelengths in the Southern Ocean of ~300 km (Hughes 1995).

We employ a suite of numerical experiments using a primitive equation model and idealized bottom topography. In section 2, the model and experiment design are explained, while section 3 explains in detail the wave activity flux diagnostic to be employed. In section 4, the model output is described, and we discuss the dynamics of the oceanic storm track in section 5, drawing on the experimental results and employing the wave activity flux to develop a dynamical framework to explain the initiation and downstream development of storm tracks. Last, the implications of this work are explored in section 6.

2. Experimental setup

a. The numerical model

We employ the Generalized Ocean Layer Dynamics (GOLD) model (Adcroft et al. 2008; Hallberg and Adcroft 2009), version Siena, which is an updated version of the Hallberg isopycnal model (Hallberg and Rhines 1996).

TABLE 1. Topography parameters for the idealized numerical experiments.

Experiment	λ_x (km)	λ_y (km)	H_o (m)
1	300	1200	2000
2 (reference)	600	1200	2000
3	1200	1200	2000
4	1800	1200	2000
5	2400	1200	2000
6	1200	1200	1000
7	1200	1200	3000

This model solves the Boussinesq primitive equations using density as the vertical coordinate. The experimental setup is similar to that of Ward and Hogg (2011): a zonally periodic β-plane channel with a zonal length of $L_x = 4800$ km, meridional width of $L_y = 2400$ km, and free-slip boundary conditions on the northern and southern walls. We use 10 adiabatic layers with a total depth of 4000 m and set the stratification such that the largest baroclinic deformation radius at initialization is $R_{d_1} = 30$ km. The grid spacings Δx, $\Delta y = 0.2 R_{d_1}$ (6 km) are set to ensure that the flow resolves the mesoscale.

$$h(x, y) = \begin{cases} 0 & |x - x_o|, |y - y_o| > \lambda_x/2, \lambda_y/2 \\ H_o \cos\left(\pi \frac{x - x_o}{\lambda_x}\right) \cos\left(\pi \frac{y - y_o}{\lambda_y}\right) & |x - x_o|, |y - y_o| \leq \lambda_x/2, \lambda_y/2 \end{cases},$$

where H_o is the maximum height of the topography; λ_x, λ_y are the respective topographic length scales in the zonal and meridional directions; and x_o, y_o are the coordinates of the center of the topography. In this study, both the zonal length λ_x and the height of the topography H_o are varied. The individual experiments undertaken using isolated topography are shown in Table 1. The topographic length scales are significantly larger than the first deformation radius, that is, λ_x, $\lambda_y \gg R_{d_1}$. The reference experiment has a zonal length scale of $\lambda_x = 600$ km and a height of $H_o = 2000$ m.

The center of the bump is located just south of the center of the domain at $y_o = L_y/2 - 200$ km. This choice has been made in order to ensure that only one of the multiple quasi-zonal jets that form in the channel is influenced by the bottom topography. When the topography was placed in the center of the domain, we found that both zonal jets would be steered by the topography, resulting in a convoluted standing wave field downstream of the bump that complicated the following analysis without adding further insight.

Our topographic profile is an idealization of the large-scale bathymetric features in the Southern Ocean. At

The Coriolis parameter under the β-plane approximation $f = f_0 + \beta y$ with $f_0 = -1 \times 10^{-4}$ s^{-1} and $\beta = 1.5 \times 10^{-11}$ m^{-1} s^{-1}, is representative of Southern Ocean latitudes. Horizontal biharmonic viscosity, with a coefficient of $A_H = 1 \times 10^{10}$ m^4 s^{-1} is used to ensure numerical stability, and a quadratic bottom drag with a dimensionless coefficient of $C_D = 3 \times 10^{-3}$ is applied.

The model is driven by a zonally uniform, zonal wind stress with a truncated sinusoidal profile, with nonzero values found across the central 80% of the channel width. As in Ward and Hogg (2011), the peak wind stress is 0.1 N m^{-2}. After spinup to a statistically steady state (which typically takes 25–30 yr of model time), the numerical experiments are run for a further 30 yr to generate a sufficiently long time series to produce reliable statistics.

b. Bottom topography

The topography is an isolated bump with variable height and zonal length scale. The topography takes the form of a sinusoid, where the height of the topography above the ocean floor at $z = -4000$ m is given by

the smallest zonal extent considered, the idealized topography is reminiscent of features with narrow zonal extent, such as the Macquarie Ridge. As λ_x increases so that $\lambda_x \approx \lambda_y$, the topography becomes more reminiscent of features like the Kerguelen Plateau. As the topography achieves its largest zonal extent, it can be thought of as an idealization of long, zonally oriented bathymetric features such as the Southeast Indian Ridge, similar to the study by Witter and Chelton (1998).

3. Diagnostics and wave activity

In this section, we describe the main diagnostics used in this paper and introduce the wave activity flux of Takaya and Nakamura (2001). This diagnostic is related to the Eliassen–Palm flux (Plumb 1985; Bühler 2014), which is in turn related to specific terms in the eddy energy budget.

a. Computation of transient eddies and EKE

To define an eddying quantity, we use the standard Reynolds decomposition. For a given field a, the angle brackets $\langle a \rangle$ denote an averaging operator used to

specify the "mean" field. "Eddies" are deviations from the mean.

We follow WWH07 by applying a temporal low-pass filter (a finite impulse response Blackman filter; Smith 2003, p. 292), which is taken as the mean flow $\langle \cdot \rangle_t$. The cutoff period is set to 180 days.[1] We assume that any flow variable a can be decomposed into mean and eddy components, where the transient eddies are defined relative to the low-pass filtered mean flow:

$$a' = a - \langle a \rangle_t. \tag{1}$$

Thus, the transient EKE density in the kth isopycnal layer, with density ρ_k, is defined as

$$\text{EKE}_k = \frac{\rho_k}{2}(u'_k u'_k + v'_k v'_k) = \frac{\rho_k}{2}\mathbf{u}' \cdot \mathbf{u}', \tag{2}$$

where $\mathbf{u} = (u, v)$ is the velocity vector.

b. Wave activity

Takaya and Nakamura (2001) derive a quasigeostrophic, phase-independent conservation law for wave activity of the form:

$$\frac{\partial M}{\partial t} + \nabla \cdot \mathbf{W} = -\mathcal{D}, \tag{3}$$

where M is the generalized *wave activity*, defined as

$$M = \rho \frac{\mathcal{A} + \mathcal{E}}{2}, \tag{4}$$

and $\mathbf{V}$ is the three-dimensional gradient operator. Here, $\mathcal{A} = q'q'/2|\nabla\langle q \rangle_t|$, where q is the quasigeostrophic potential vorticity. The quantity $\mathcal{A}$ is thus the eddy enstrophy divided by the background potential vorticity gradient, which is equal to the pseudomomentum (Plumb 1985). The equation $\mathcal{E} = e/(|\langle \mathbf{u} \rangle_t| - c_p)$ describes the total eddy energy density e (kinetic plus potential), normalized by the phase speed of the eddies c_p [called "waves" in Takaya and Nakamura (2001)], relative to the speed of the mean flow $|\langle \mathbf{u} \rangle_t|$. The term $\mathcal{D}$ represents the nonconservative dissipation terms. When $\partial M/\partial t > 0$, the eddying flow increases its magnitude at the expense of the mean flow.

The vector $\mathbf{W}$ represents the wave activity flux. In isopycnal coordinates, the components of $\mathbf{W}$ are

$$\mathbf{W} = \rho \begin{bmatrix} W_x \\ W_y \\ W_\rho \end{bmatrix} = \frac{\rho}{2|\langle \mathbf{u} \rangle_t|} \left\{ \begin{array}{l} \langle u \rangle_t \left(v'_g v'_g - \psi'_g \dfrac{\partial v'_g}{\partial x} \right) - \langle v \rangle_t \left(v'_g u'_g + \psi'_g \dfrac{\partial v'_g}{\partial y} \right) \\[12pt] \langle u \rangle_t \left(-u'_g v'_g + \psi'_g \dfrac{\partial u'_g}{\partial x} \right) + \langle v \rangle_t \left(u'_g u'_g + \psi'_g \dfrac{\partial u'_g}{\partial y} \right) \\[12pt] \dfrac{f_0^2 \rho_0}{g_0} \left[\langle u \rangle_t \left(-v'_g \dfrac{\partial \psi'_g}{\partial \rho} + \psi'_g v'_g \right) + \langle v \rangle_t \left(-u'_g \dfrac{\partial \psi'_g}{\partial \rho} + \psi'_g \dfrac{\partial u'_g}{\partial \rho} \right) \right] \end{array} \right\} + M\langle \mathbf{C}_u \rangle_t. \tag{5}$$

The gradient operator is written as $\mathbf{V} = (\partial/\partial x, \partial/\partial y, 1/\sigma_0 \partial/\partial \rho)$, where the constant σ_0 term (defined below) is moved from outside of the gradient operator to ensure that all components of $\mathbf{W}$ have the same units. More details of the derivation are given in the appendix.

In Eq. (5), $\langle \mathbf{C}_u \rangle_t$ is the low-pass filtered (mean) phase velocity of the perturbations in the direction of $\langle \mathbf{u} \rangle_t$. The quantity ψ'_g is the geostrophic streamfunction, which in isopycnal coordinates is related to the Montgomery potential ϕ by $\psi'_g = \phi'/f_0$ (Berrisford et al. 1993). The parameter g_0 is the gravitational acceleration, while the subscript "g" refers to geostrophic quantities. The variable ρ_0 is some reference density, $\sigma_0 = \partial z_0/\partial \rho$ is the background thickness density, and z_0 is the isopycnal

layer interface depth. The constant σ_0 represents the "reference" state, which is perturbed in forming the quasigeostrophic equations. The first term on the right-hand side of Eq. (5) is the wave activity flux due to the stationary disturbances, while the second term on the right-hand side is the wave activity flux due to the propagation of disturbances.

The phase independence of M and $\mathbf{W}$ means that, unlike eddy energy budgets or the Eliassen–Palm flux, this wave activity is not dependent on the choice of averaging operator. The lack of either spatial or temporal averaging is an important consideration, as a spatially averaged diagnostic cannot represent propagation in the direction of the averaging operator, while time averaging precludes the representation of stationary disturbances.

In formulating Eq. (3), Takaya and Nakamura (2001) invoked the quasigeostrophic approximation, which is applicable to the Southern Ocean. Although we use

---

[1] We have tested a variety of cutoff periods, and, provided that the cutoff period is less than ~1.5 yr, the results are qualitatively similar.

a primitive equation model that solves the non-quasigeostrophic equations, the experimental design mimics a Southern Ocean parameter regime, with a Rossby number Ro of ~0.05 and Richardson number Ri of ~200; both conditions for the validity of the quasigeostrophic approximation [Ro $\ll$ 1 and $(\text{RiRo})^{-1} \ll 1$] (Berrisford et al. 1993) are met away from topography. Although linear dynamics are assumed in the derivation of Eq. (5), the wave-activity flux has been used successfully in the analysis of nonlinear eddies (Danielson et al. 2006).

c. Physical description of the wave activity flux

As the wave activity flux is not a familiar tool in oceanography (Bühler 2014), we now review the dynamical interpretation of **W** using an "argument by analogy" to compare the individual terms in Eq. (5) to those that arise in energy budget calculations more familiar to oceanographers. Although Takaya and Nakamura (2001) also provided a detailed physical interpretation of the wave activity flux, their approach assumes a familiarity with atmospheric dynamics and does not make explicit comparison with the energy budget.

Energy budget calculations, which track changes between mean and eddy kinetic and potential energies (PEs), give similar insight to wave activity fluxes (Danielson et al. 2006). Energy budgets are used commonly in oceanography to identify important physical processes (Aiki and Yamagata 2006; Aiki and Richards 2008; Hughes et al. 2009), although they are generally presented in a global integral form rather than the local

forms used in this paper. Plumb (1983) has demonstrated that the energy cycle has limited utility as a diagnostic tool: individual terms within the energy budget are nonunique, and mathematical manipulation of the energy equations can lead to energy fluxes being interpreted as energy conversions (and vice versa). Indeed, Plumb (1983, p. 1685) warns that "...one cannot place any absolute significance on *individual* flux or conversion terms; these terms only have their allotted meaning in the context of a particular scheme." Hence, a wave activity flux may be a preferable tool for the diagnosis of local dynamics.

The wave activity M of Eq. (4) is a weighted sum of total perturbation energy. It has been shown by Plumb (1985) and Takaya and Nakamura (2001) that, in the WKB limit, the wave activity propagates at the Rossby group velocity, which is also the propagation speed of energy emitted by Rossby waves. Son et al. (2009) and Danielson et al. (2006) have shown that M correlates strongly with regions of elevated eddy activity. These studies suggest the use of eddy energy as an analogy to explain the wave activity, although the two should not be considered equivalent.

We define the mean and eddy kinetic energies as $K_m = 0.5|\langle \mathbf{u} \rangle_t|^2$ and $K_e = 0.5|\mathbf{u}'|^2$, respectively. Determination of the time evolution equations for the quasigeostrophic mean and eddy energy is found in numerous sources (e.g., Pedlosky 1987, section 3.21). The mean energy budget is [ignoring small cross terms as in Orlanski and Katzfey (1991)]

$$\underbrace{\left(\frac{\partial K_m}{\partial t} + \langle \mathbf{u} \rangle_t \cdot \mathbf{\nabla}_H K_m\right)}_{\text{MKE Tendency/Advection}} + \mathbf{\nabla}_H \cdot \underbrace{(\langle u \rangle_t \langle u' \mathbf{u}' \rangle_t + \langle v \rangle_t \langle v' \mathbf{u}' \rangle_t + \langle \mathbf{u} \rangle_t \langle p \rangle_t)}_{\text{MKE Flux}}$$
$$= \underbrace{(\langle u' \mathbf{u}' \rangle_t \cdot \mathbf{\nabla}_H \langle u \rangle_t + \langle v' \mathbf{u}' \rangle_t \cdot \mathbf{\nabla}_H \langle v \rangle_t)}_{\text{EKE} \rightarrow \text{MKE}} + \underbrace{\langle w \rangle_t \langle b \rangle_t}_{\text{MPE} \rightarrow \text{MKE}} + \underbrace{\langle \mathbf{u} \rangle_t \cdot \langle \mathbf{F} \rangle_t}_{\text{External work}}, \tag{6}$$

where w is the vertical component of velocity, p is the dynamic pressure, z is the depth, b is the buoyancy, and **F** is the nonconservative body force. The term $\mathbf{\nabla}_H = (\partial_x, \partial_y)$ is the horizontal gradient operator. We have used geometric height z as the vertical coordinate

for simplicity in the derivation. The extension to isopycnal coordinates is more involved and can be found in Bleck (1985) and Aiki and Yamagata (2006), but does not change the result significantly. The time evolution equation for the eddy kinetic energy K_e can be written as

$$\underbrace{\left[\frac{\partial K_e}{\partial t} + (\langle \mathbf{u} \rangle_t + \mathbf{u}') \cdot \mathbf{\nabla}_H K_e\right]}_{\text{EKE Tendency/Advection}} + \underbrace{\mathbf{\nabla}_H \cdot (\langle \mathbf{u}' p' \rangle_t) + \frac{\partial}{\partial z}(\langle p' w' \rangle_t)}_{\text{EKE Flux}} = \underbrace{-(\langle u' \mathbf{u}' \rangle_t \cdot \mathbf{\nabla}_H \langle u \rangle_t + \langle v' \mathbf{u}' \rangle_t \cdot \mathbf{\nabla}_H \langle v \rangle_t)}_{\text{EKE} \rightarrow \text{MKE}}$$
$$+ \underbrace{w' b'}_{\text{EPE} \rightarrow \text{EKE}} + \underbrace{\mathbf{u}' \cdot \mathbf{F}'}_{\text{External work}}. \tag{7}$$

Following Plumb (1983) and Gent and McWilliams (1990), we use a local available potential energy diagnostic that is able to represent both eddy and mean potential energies spatially and temporally. The eddy potential energy (EPE) can be defined as

$$P_e = \frac{b'b'}{\partial \langle b \rangle_t / \partial z},$$ (8)

with the definition of the mean following from the decomposition of the total potential energy, that is, $P_m = P_{\text{total}} - P_e$. The eddy potential energy budget is thus

$$\underbrace{\left[\frac{\partial P_e}{\partial t} + (\langle \mathbf{u} \rangle_t + \mathbf{u}') \cdot \nabla_H P_e \right]}_{\text{EPE Tendency/Advection}}$$

$$= \underbrace{(-w'b')}_{\text{EPE} \to \text{EKE}} - \underbrace{\left[b' \mathbf{u}' \cdot \nabla_H \left(\frac{\langle b \rangle_t}{\partial \langle b \rangle_t / \partial z} \right) \right]}_{\text{EPE} \to \text{MPE}},$$ (9)

with a similar expression for the mean PE:

$$\underbrace{\left(\frac{\partial P_m}{\partial t} + \langle \mathbf{u} \rangle_t \cdot \nabla_H P_m \right)}_{\text{MPE Tendency/Advection}} + \underbrace{\left[\nabla_H \cdot \left(\langle \mathbf{u}'b' \rangle_t \frac{\partial \langle b \rangle_t}{\partial z} \right) \right]}_{\text{MPE Flux}}$$

$$= \underbrace{\left[b' \mathbf{u}' \cdot \nabla_H \left(\frac{\langle b \rangle_t}{\partial \langle b \rangle_t / \partial z} \right) \right]}_{\text{EPE} \to \text{MPE}} - \underbrace{(\langle w \rangle_t \langle b \rangle_t)}_{\text{MPE} \to \text{MKE}}.$$ (10)

The terms within energy budgets have simple physical interpretations. Terms that appear in two equations that have opposite sign but are otherwise identical are interpreted as a conversion of energy from one form to another. Conversion terms on the right-hand side of Eqs. (6), (7), (9), and (10) are annotated with the energy pathway. In our study, we are primarily concerned with the conversion of mean potential energy (MPE) to eddy potential energy described by buoyancy flux [term labeled EPE → MPE in Eqs. (9) and (10)] and the conversion of eddy potential energy to eddy kinetic energy by buoyancy production [term labeled EPE → EKE in Eqs. (7) and (9)]. Taken together, these two terms are frequently associated with the production of EKE by the baroclinic instability process.

The fluxes of each energy type are also annotated in the energy budgets above. We are primarily concerned with the flux of EKE, written as $\nabla_H \cdot (p'\mathbf{u}')$. Physically, this term represents the rate of work done by the pressure fluctuations. As the geostrophic component of the flow is nondivergent and parallel to the streamfunction, only the ageostrophic flow contributes to this flux of energy, such that

$$\nabla_H \cdot (p'\mathbf{u}') = \nabla_H \cdot (p'\mathbf{u}'_a),$$ (11)

where $\mathbf{u} = \mathbf{u}_g + \mathbf{u}_a$, and $\mathbf{u}_a$ is the ageostrophic velocity. Energy flux vectors are discussed extensively in Pedlosky (1987, section 6.10).

1) HORIZONTAL COMPONENTS OF **W**

The components of the wave activity flux **W** in the horizontal direction have two forms. The first form represents the transport of momentum due to the perturbation correlations. These terms take the form of perturbation momentum correlations:

$$\begin{bmatrix} \langle u \rangle_t (v'_g v'_g) + \langle v \rangle_t (-u'_g v'_g) \\ \langle u \rangle_t (-u'_g v'_g) + \langle v \rangle_t (u'_g u'_g) \end{bmatrix}.$$

Following Takaya and Nakamura (2001), these terms are related to the flux of perturbation momentum by the mean flow. Comparing these terms to the first conversion term within the mean and eddy kinetic energy budgets [Eqs. (6) and (7), labels EKE → MKE], it can be seen that the divergence of this wave activity flux term corresponds to conversion from mean to eddy kinetic energies through shear production.

The other terms that contribute to the horizontal wave activity flux have the form

$$\begin{bmatrix} -\langle u \rangle_t \left(\psi'_g \dfrac{\partial v'_g}{\partial x} \right) - \langle v \rangle_t \left(\psi'_g \dfrac{\partial v'_g}{\partial y} \right) \\ \langle u \rangle_t \left(\psi'_g \dfrac{\partial u'_g}{\partial x} \right) - \langle v \rangle_t \left(\psi'_g \dfrac{\partial u'_g}{\partial y} \right) \end{bmatrix}.$$

These terms are slightly more difficult to interpret. Following Orlanski and Sheldon (1995), who show that if the perturbations are small-amplitude waves traveling in the x direction with phase speed c_p, we write

$$\psi'_g \frac{\partial v'_g}{\partial x} \approx - \left[\frac{1}{\langle u \rangle_t - c_p} + \frac{\beta y}{f_0(\langle u \rangle_t - c_p)} \right] p'u'_a.$$ (12)

Similar expressions can be derived for the other terms with the same form in **W**. Although Eq. (12) is only approximate, it serves to illustrate the relationship between the wave activity flux and the ageostrophic fluxes of pressure. Comparing Eq. (12) with the flux term in the EKE budget of Eq. (11), we can see that the second term that contributes to the horizontal wave activity flux is related to the transport of EKE by the pressure work done by the ageostrophic flow, scaled by the phase speed of transient eddies relative to the mean flow.

The horizontal wave activity flux can be thought of as analogous to the flux of KE. The first term in the horizontal component of **W** is related to the flux of perturbation momentum by the mean flow, while the second term is related to the flux of EKE by the pressure work due to the ageostrophic flow.

2) VERTICAL COMPONENTS

The first term in the vertical component of **W** has the form (in z coordinates):

$$\langle u \rangle_t \left(-v'_g \frac{\partial \psi'_g}{\partial z} \right) - \langle v \rangle_t \left(u'_g \frac{\partial \psi'_g}{\partial z} \right),$$

which with application of the hydrostatic equation $\partial p/\partial z = -b$ becomes

$$f_0^{-1}[-\langle u \rangle_t (v'_g b') + \langle v \rangle_t (u'_g b')].$$

This term is a covariance of the perturbation buoyancy and horizontal velocity and constitutes a measurement of the eddy buoyancy flux. The eddy buoyancy flux appears in the potential energy budgets [Eqs. (9) and (10)] as the conversion from EPE to MPE. Vertical wave activity fluxes represent regions where the energy is being converted between the background PE reservoir to the local EPE field, which can be used to identify regions of baroclinic eddy growth.

The final term in the vertical component of the wave activity can be shown to be related to the vertical flux of EKE because of the pressure work, as described above for the second term that contributes to the horizontal components of **W**. This term plays no role in this study, as is explained below.

3) ISOPYCNAL COORDINATES

In isopycnal coordinates, the physical interpretation of the horizontal components of **W** does not require significant modification. However, the term that corresponds to the EKE flux due to the ageostrophic pressure flux is replaced by ageostrophic flux of Montgomery potential:

$$p'\mathbf{u}'_a \to \phi'\mathbf{u}'_a.$$

The vertical components of **W** also have a similar interpretation in isopycnal coordinates as in z coordinates. First, in an adiabatic fluid, such as our model, the isopycnal velocity $\dot{\rho}$ vanishes, as diabatic terms are required to force fluid parcels across isopycnals. As such, there is no cross-isopycnal flux of EKE due to pressure work.

The term that can be interpreted as the flux of buoyancy in z coordinates is instead interpreted as the horizontal mass flux:

$$-(v'_g, u'_g)b' \to \frac{g_0}{\rho_o}(v'_g, u'_g)\sigma',$$

where σ is the isopycnal layer thickness density $\partial z/\partial\rho$, which is often referred to as just "thickness." Horizontal thickness flux plays the same role in the baroclinic instability process in isopycnal coordinates as heat or buoyancy flux plays in z coordinates: acting to either steepen or relax isopycnal slopes (Gent and McWilliams 1990; Grotjahn 2003). Thus, like in z coordinates, the vertical component of **W** is a useful tool for diagnosing regions of baroclinic energy conversion.

d. A note on vertical averaging

Throughout this paper, we report numerous vertically averaged quantities. In isopycnal coordinates, all vertically averaged quantities are thickness weighted. For a quantity a_k in layer k, the vertical average is

$$\overline{a} = \sum_{k=1}^{N} \sigma_k a_k \bigg/ \sum_{k=1}^{N} \sigma_k, \qquad (13)$$

where N is the number of layers, and σ_k is the layer thickness.

4. Model results

a. Basic state

The time-mean basic state for the reference experiment (zonal topographic length scale $\lambda_x = 600$ km) is shown in Fig. 2. The mean fields from these experiments are qualitatively similar to other experiments listed in Table 1. The time-mean zonal velocity (Fig. 2a) shows two strong zonal jets. The jet in the northern part of the domain is not significantly influenced by topography, while the jet to the south of the domain is strongly steered. East of the topography a standing meander forms, which is most clearly seen in the meridional velocity field (Fig. 2b). The standing meander has a wavelength of approximately 550 km (confirmed by spectral analysis), which is close to the expected wavelength obtained using appropriate values for $\langle u \rangle_t$ in the Rossby wave dispersion relationship (Held 1983).

The transient EKE field computed by the method described in section 3a is shown in Fig. 2c. Two storm tracks are evident: the northern storm track follows the core of the northern jet and does not vary with longitude, and the southern storm track forms downstream of the topography, peaks and slowly decays, which is reminiscent of storm tracks in the Southern Ocean (see Fig. 1b). We restrict our attention to the topographically influenced storm track to the south. Both the
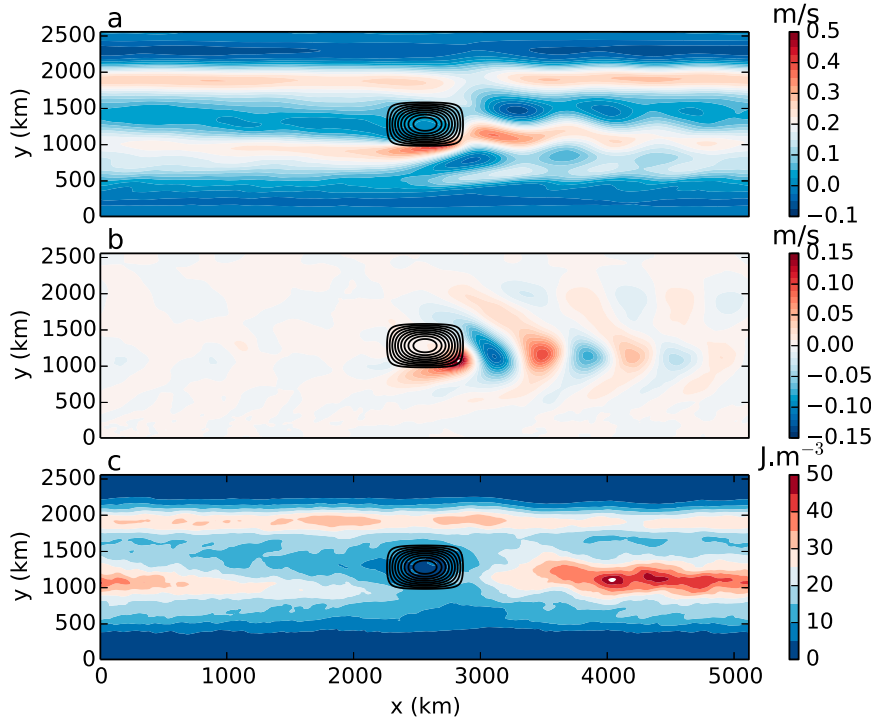
FIG. 2. Time-mean, vertically averaged (a) zonal velocity, (b) meridional velocity, and (c) transient EKE for the reference experiment (expt 2 shows zonal topographic length λ_x of 600 km). Solid black lines show topographic height above the model ocean floor at $z = -4000$ m [contour interval (CI) is 200 m].

mean flow and the EKE field are approximately equivalent barotropic.

The kinematics of the storm track are investigated by averaging the meridional velocity and the transient EKE between latitudes that bound the storm track (between $y = 700$ km and $y = 1350$ km), shown in Fig. 3. The averaged meridional velocity (Fig. 3a) forms a stationary wave train that commences immediately downstream of the topography, with a wave crest being found at $x \simeq 2800$ km, close to the edge of the hill. We have compared the spatial pattern of v produced in our model with simple, barotropic linear calculations described in Held (1983) (not shown) and found agreement in the wavelength of the stationary meander and its meridional propagation, although this required some tuning of the friction parameter in the linear model.

In contrast, the transient EKE (Fig. 3b) does not peak until ~1000 km downstream of the topography and slowly decays farther to the east. To measure the length of the storm track, we have modified the procedure of Kaspi and Schneider (2013). We define the start of the storm track as the maximum of the meridionally averaged transient EKE. To determine the downstream extent of the storm track, the meridionally averaged EKE is smoothed using a Gaussian filter with a very large

standard deviation (300 grid points or 1800 km). The point at which the unsmoothed EKE falls below the smoothed EKE is declared the terminal point of the storm track. Storm-track lengths are estimated by this method for experiments 1 through 5.

Figure 4a shows the storm-track length and the amplitude of the stationary wave as a function of λ_x. In each case, we see that as the topography becomes longer, both the wave amplitude and the storm-track length decrease, although there is an exception at $\lambda_x = 600$ km, where the wave amplitude is at its maximum. This value of λ_x is approximately equal to half the wavelength of the standing meander, implying near resonance. The relationship for both quantities is weak; although λ_x varies by a factor of 8, the resultant change in the wave amplitude is only a factor of 2, with similar scaling for the storm-track length. We also compute the storm-track intensity for each experiment by meridionally averaging the (time averaged) EKE over the storm track (Fig. 4b, + symbols). We find no dependence of this quantity on the length scale of the topography. The maximum zonal velocity at a point just upstream of the topography (Fig. 4b, ▲ symbols) is also not sensitive to varying λ_x.

The effect of topography height on the storm-track length and intensity was also investigated. As summarized
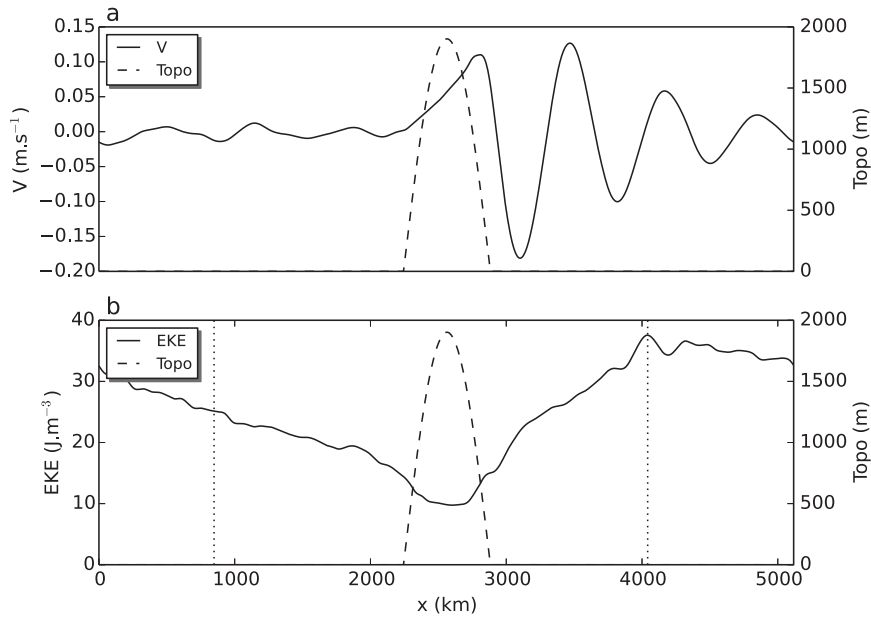
FIG. 3. Transects of time-mean, vertically averaged (a) meridional velocity and (b) EKE (solid), with topographic height above the model ocean floor (dashed) for the reference experiment (topography length λ_x of 600 km). Dotted vertical lines indicate the start and end of the storm track as determined by the method described in section 4.

in Table 1, the height of the bump is varied from 1000 to 3000 m, while the zonal length has been held constant at 1200 km. Surprisingly we find no significant changes or trends in either storm-track length or intensity as we

varied the height of the topography. This result is in contrast to previous work on atmospheric storm tracks by Son et al. (2009), who found weak sensitivity of storm-track intensity to changing topographic height
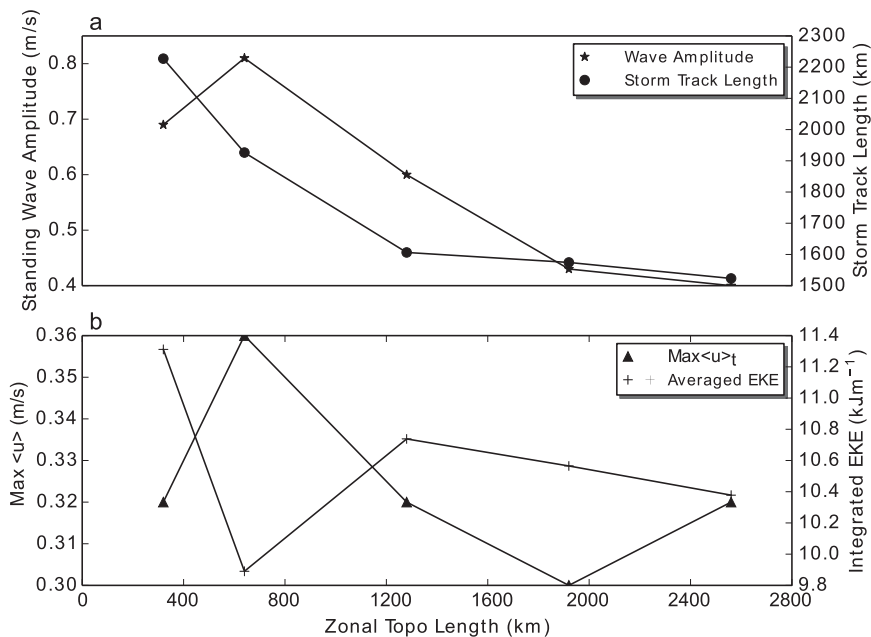
FIG. 4. (a) Amplitude of the stationary meander (stars) and storm-track length (solid circles) and (b) maximum zonal velocity just upstream of the topography (triangles) and EKE spatially averaged over the storm track (plus signs) as a function of zonal topographic length λ_x.

(although the result is strongly dependent on the state of the upstream jet).

b. Spatial scales of the standing meander and transient eddies

In the midlatitude atmosphere, there is very little length scale separation between standing and transient eddies (Kaspi and Schneider 2013). This lack of scale separation affects the dynamics of the storm-track initiation and downstream development. However, in the ocean there is thought to be substantial scale separation between standing and transient eddies (WWH07). In this section, we calculate the length scales present in each eddy component.

For each experiment we compute the wavelength of the standing meander using a fast Fourier transform. The wavelength is approximately equal for each experiment, being ~550 ± 50 km. This is as expected, as downstream of the topography, the stationary Rossby wave wavenumber will be set by the dispersion relationship:

$$K^2 = \frac{\beta}{\langle u \rangle_t}, \tag{14}$$

where $K = \sqrt{k^2 + l^2}$ is the total wavenumber.

To determine the spatial scale of transient eddies, we use a series of adjacent bandpass filters applied in the spatial domain. The filter cutoff wavenumbers are specified on total wavenumber K, defining an annulus in two-dimensional wavenumber space, where the internal radius corresponds to the low wavenumber cutoff and the outer radius corresponds to the high wavenumber cutoff. The passbands are chosen to ensure that their area in wavenumber space is equal, a procedure similar to discrete wavelet analysis (Farge 1992). Applying the filter in the spatial domain with passbands of equal area ensures that the results of each filtering operation can be directly compared. We use passbands that cover at least three adjacent wavenumber bins, which enable sufficient resolution at small wavenumbers.

Each bandpass filter is applied at every time step, and the EKE is integrated over the storm track to give a measure of the relative contribution that the scales within the passband make to the total energy of the storm track. The time average EKE scale decomposition for the reference experiment [experiment (expt) 2)] is presented in Fig. 5. Results do not vary substantially between experiments. There is a significant peak in Fig. 5, indicating that EKE is concentrated at length scales of ~190 km, which is approximately equal to $2\pi R_{d_1}$ (since $R_{d_1} \approx 30$ km in this model).

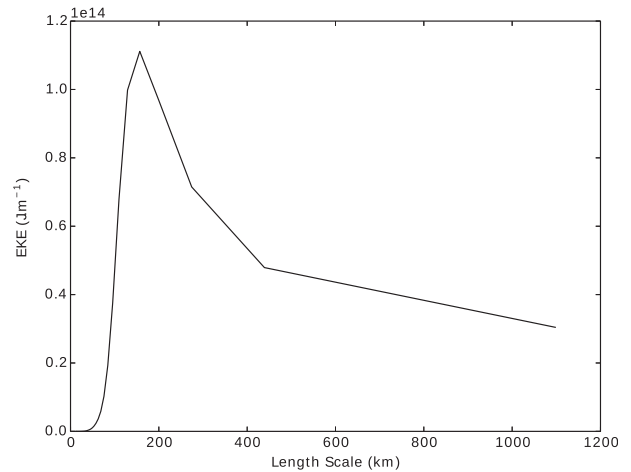The calculations show a clear scale separation between the standing and transient eddies. This scale

FIG. 5. Energy/length scale decomposition for the reference experiment (expt 2, λ_x of 600 km).

separation has implications for the dynamics of oceanic storm tracks, which will be discussed in the next section.

5. Storm-track dynamics

To investigate the dynamics of the storm tracks, we employ the generalized wave activity defined in Eqs. (3) and (5). Recall from section 3 that the wave activity M is analogous to eddy energy, while the wave activity flux $\mathbf{W}$ is useful for identifying regions of baroclinic eddy growth and the flux of EKE. To compute the wave activity flux, geostrophic velocities are calculated by estimating the derivative of the Montgomery potential using centered differencing. To compute the contribution of the propagating eddy component, $M\langle \mathbf{C}_u \rangle_t$ in Eq. (5), we use the method of Lee and Cornillon (1996) for tracking propagating features to determine the phase speed in the alongstream direction. We find that $\langle \mathbf{C}_u \rangle_t$ is generally small, and the propagating component has negligible impact on the total M budget. As such, we present the results only for the stationary component of $\mathbf{W}$.

The time-mean horizontal components of $\mathbf{W}$ are shown as vectors in Fig. 6 along with the transient EKE for experiments with increasing λ_x. The result for $\lambda_x = 300$ km is presented in Fig. 6a, $\lambda_x = 1200$ km in Fig. 6b, and $\lambda_x = 2400$ km in Fig. 6c. In each case, horizontal wave activity fluxes show convergence just downstream of the topography in regions where $d\text{EKE}/dx > 0$ and upstream of the maximum of EKE. There is no evidence of wave activity flux upstream of the topography entering the storm-track region, although there is some evidence of wave activity flux from the northern storm track entering the southern storm-track region. This result suggests that the wave activity is mostly generated locally in the lee of the topography.
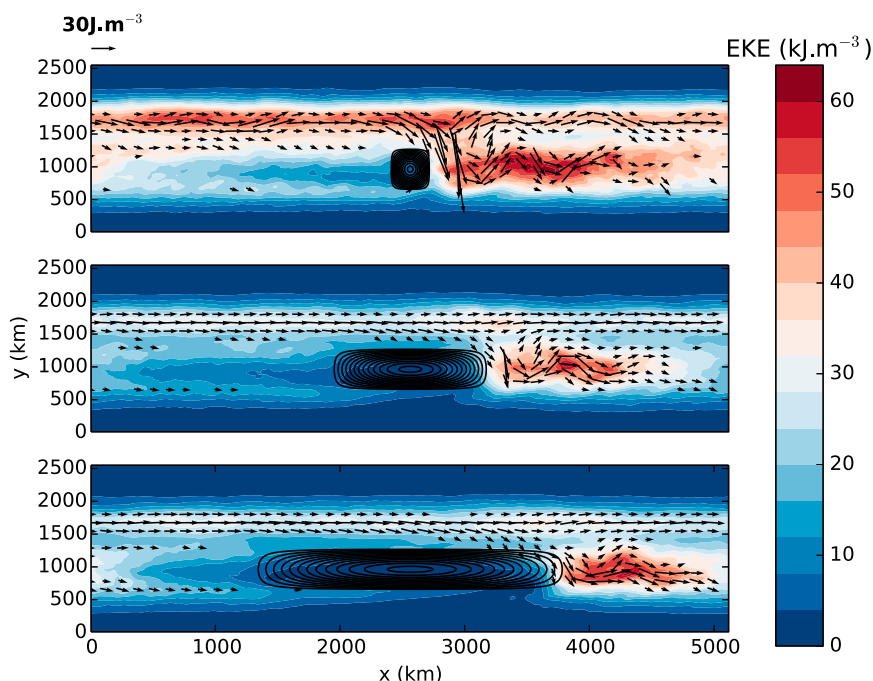
FIG. 6. Time-averaged, vertically averaged transient EKE (colored contours) with time-mean vectors of the horizontal components of the wave activity flux (arrows) for experiments (a) 1 ($\lambda_x = 300$ km), (b) 3 ($\lambda_x = 1200$ km), and (c) 5 ($\lambda_x = 2400$ km).

Within the storm-track regions farther downstream of the topography, wave activity flux vectors are well organized in the zonal direction, although there is some meridional flux of wave activity due to the influence of the standing wave. This meridional flux becomes greater as the zonal topographic length scale decreases, as does the amplitude of the standing meander (see Fig. 4). There is no strong, two-dimensional convergence or divergence of the horizontal wave activity flux downstream of the peak EKE, a result similar to those of Orlanski and Chang (1993).

a. Storm-track initiation

Recall from section 3 that the vertical component of the wave activity flux W_ρ can be used to diagnose the conversion of mean potential energy to eddy potential energy by the baroclinic instability process. Plotted in Fig. 7a is the time-mean, vertically averaged W_ρ for the reference experiment ($\lambda_x = 600$ km) downstream of the topography ($x > L_x/2$). In Fig. 7, regions of positive vertical wave flux (which correspond to regions of enhanced baroclinic energy conversion) are found at $x \approx 3000$ km and $x \approx 3400$ km, while there is a narrow region of negative flux at $x \approx 3250$ km. To determine a mechanism for the localized influence of W_ρ, we add to Fig. 7a contours of meridional velocity, which show the phase lines of the stationary meander.

Integrating the vertically averaged, time-mean W_ρ and v meridionally between latitude bands that approximately bound the northern and southern edges of the storm track at $y = 700$ and 1500 km (Fig. 7b), we find two distinct regions where W_ρ is greater than zero between $x \approx 2700$ and 3100 km and again between $x \approx 3300$ and 3500 km. The EKE (Fig. 7c) rises from a minimum at the end of the topography at $x \approx 2900$ km until it reaches its maximum value at $x \approx 4000$ km. In this EKE growth region, we also find large, positive (upward) W_ρ flux and the strongest stationary meander amplitudes. As the meander amplitude decreases, so too does the EKE growth and the vertical flux of wave activity. Downstream of the maximum EKE, $W_\rho \approx 0$.

The analysis of W_ρ indicates that strong mean PE to eddy PE conversion occurs downstream of the topography. This region also coincides with a region of $d(\text{EKE})/dx > 0$, indicating baroclinic eddy growth downstream. Outside of the region strongly influenced by the standing meander, there is little evidence of strong mean PE to eddy PE conversion, indicating that baroclinic eddy growth is occurring primarily in the standing wave region.

This result suggests that in this model, the storm track is initiated by the stationary meander in the vicinity of the topography, yet the standing wave has minimal influence in the development of the storm track downstream of EKE growth region. This result is consistent
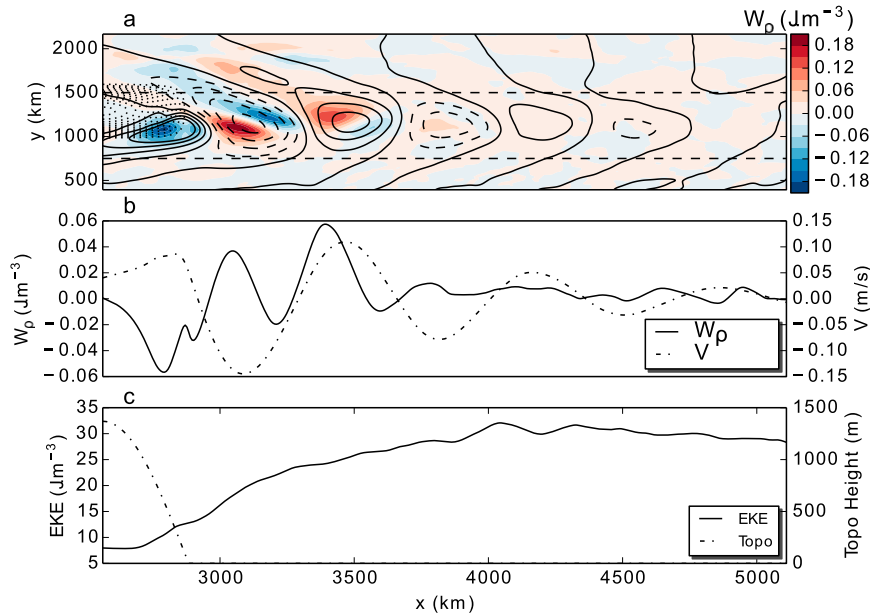
FIG. 7. (a) Time-mean, vertically averaged vertical wave activity flux (colored contours), meridional velocity (solid lines; CI = 0.05 m s^{-1}), and topographic height (dotted lines; CI = 100 m); (b) wave activity flux (solid) and meridional velocity (dashed) meridionally averaged between $y = 750$ and 1500 km (indicated by dotted horizontal lines in (a); and (c) time-mean, vertically averaged EKE (solid) and bottom topography (dashed) meridionally averaged between $y = 750$ and 1500 km. Data shown for the reference experiment (expt 2, $\lambda_x = 600$ km).

with the results of both Bischoff and Thompson (2014) and Abernathey and Cessi (2014). Both of these studies used an eddy decomposition procedure to show that the standing meander acts to steepen isopycnals through anomalous, upgradient heat flux and that the process occurs upstream of the maximum EKE. Our complementary metric tells the same story. These results are contrary to those of Kaspi and Schneider (2013), who found that in an atmospheric GCM the shape of the storm track was strongly influenced by the standing wave, even outside the region of initial transient eddy growth region.

b. Downstream development and maintenance

We now seek to understand the dynamics of the storm track downstream of the EKE growth region, where, although $d(\mathrm{EKE})/dx > 0$, the EKE remains anomalously high. Referring to Fig. 6, we see that within the storm-track regions, horizontal wave activity flux vectors are primarily oriented in the zonal direction and coincide with the regions of high EKE. As EKE decreases downstream of its peak, so too does the wave activity flux. We explore the connection between the downstream development of the storm track and **W** further in Fig. 8, where we plot the vertically averaged zonal component of **W**, meridionally averaged across

the storm-track latitudes ($y = 700$ km to $y = 1500$ km), together with the EKE for experiments 1 through 5. In each case, W_x is correlated with the EKE, in several cases matching the shape of the downstream EKE curve closely.

Both EKE and W_x decay downstream of the peak EKE, with $\partial W_x/\partial x \approx\, < 0$ and $\partial(\mathrm{EKE})/\partial x$. In a steady state ($\partial/\partial t \to 0$), there is a local balance of wave activity flux divergence and dissipation, which can be shown time averaging Eq. (3) and assuming that $\partial\langle M\rangle_t/\partial t \approx 0$:

$$\langle \mathbf{V} \cdot \mathbf{W}\rangle_t = -\langle \mathcal{D}\rangle_t, \tag{15}$$

that is, the maintenance of elevated wave activity (or EKE) against frictional dissipation in the absence of external forcing requires convergence of wave activity transport. Hence, in our simple system, it appears that wave activity propagates into the downstream storm-track regions by the ageostrophic flux of Montgomery potential, where it is converted to EKE. In a steady state, the wave activity flux convergence balances the nonconservative dissipation and meridional flux of wave activity out of the storm-track region.

To determine which physical process is responsible for the propagation of wave activity downstream, we have computed the components of the wave activity flux corresponding to the Reynolds stresses and EKE flux via
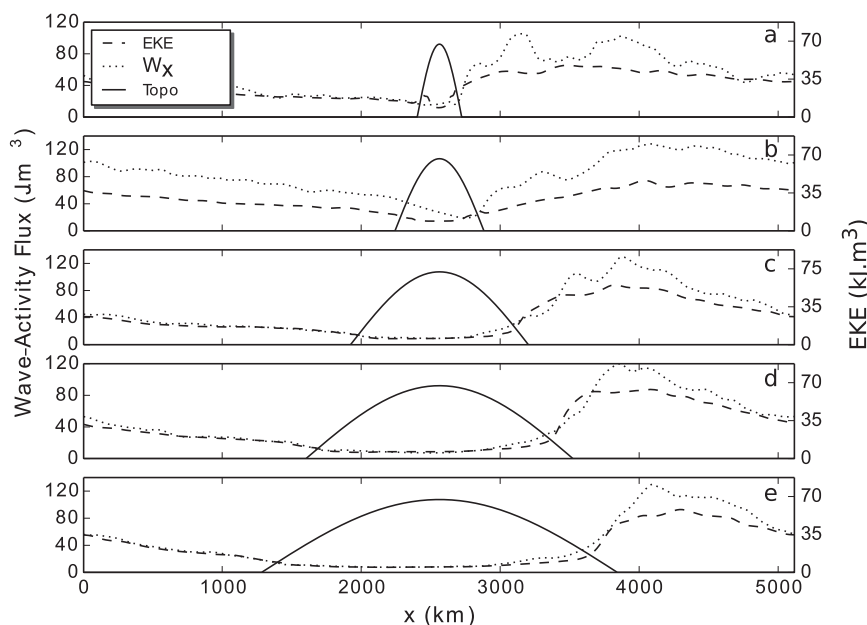
FIG. 8. Meridionally and vertically averaged, time-mean, transient EKE (dashed) with time-mean zonal component of the wave activity flux (dotted–dashed) and topography (solid) for (a) expt 1 ($\lambda_x = 300$ km), (b) expt 2 ($\lambda_x = 600$ km), (c) expt 3 ($\lambda_x = 1200$ km), (d) expt 4 ($\lambda_x = 1800$ km), and expt 5 ($\lambda_x = 2400$ km). Maximum topographic height is 2000 m (scale not shown).

the ageostrophic Montgomery potential flux. For all experiments, it is found that the ageostrophic Montgomery potential flux is dominant in the region downstream of the EKE maxima.

The analysis provided in this section indicates that the mechanism for the development of transient baroclinic eddies downstream of the baroclinically unstable regions induced by the stationary meander in our model is the downstream dispersion of EKE by the ageostrophic Montgomery potential flux. Chang and Orlanski (1993) identified EKE as the dominant factor in the downstream development in atmospheric storm tracks and our analysis suggests that the same process may be important in the Southern Ocean.

c. A physical mechanism for oceanic storm tracks

Analysis of the results of our numerical experiments using our wave activity flux diagnostic has revealed that the storm track can be divided into two regimes. The two regimes are presented schematically in Figs. 9a and 9c:

 (i) a "growth regime" immediately downstream of the topography, characterized by the EKE rapidly growing downstream and vertical wave activity flux, with $d(\text{EKE})/dx > 0$; and
(ii) a "downstream development regime," found downstream of the growth regime, characterized by slowly decaying EKE and predominantly horizontal wave activity flux, with $d(\text{EKE})/dx < 0$.

The transition from the growth regime to the downstream development regime occurs at $d(\text{EKE})/dx = 0$. The dominant physical processes in each regime are revealed by the wave activity flux. Using this analysis we propose a mechanism to explain the physics of the oceanic storm-track behavior as follows:

 (i) The interaction of the mean eastward jet with the topography acts to induce a forced, stationary Rossby wave.
(ii) In the growth regime, the stationary wave acts to increase the horizontal eddy mass flux in a manner that converts energy from the mean PE field to the eddy PE field. The energy conversion is diagnosed by the presence of upward wave activity flux vectors. Baroclinic eddy growth occurs in this environment.
(iii) Eddies grow downstream until they reach their maximum strength. Storm-track eddies flux energy into the downstream development regime by the ageostrophic flux of Montgomery potential, diagnosed by the presence of horizontally oriented wave activity flux vectors.
(iv) The storm track develops downstream of the growth regime into the downstream development regime due to the continued, convergent flux of EKE by ageostrophic Montgomery potential. This process maintains the storm track well downstream of the region where eddy growth is due to the baroclinic conversion.
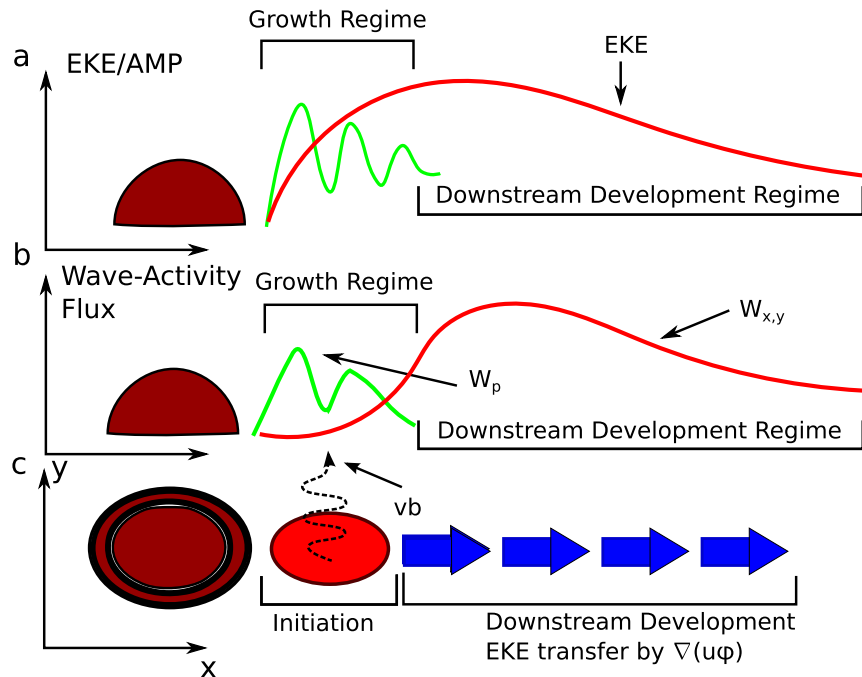
FIG. 9. Schematic of the proposed mechanism for oceanic storm-track formation: (a) zonal transect showing the basic structure of the EKE (red) and standing wave field (green) as revealed by the numerical experiments; (b) zonal transect showing the horizontal (red) and vertical (green) wave activity flux; and (c) plan view indicating the growth regime of the storm track, where eddies grow by baroclinic conversion, and the downstream development regime where ageostrophic Montgomery potential flux–induced energy transport dominates. Topography is indicated by the brown hill.

This mechanism closely mirrors those mechanisms identified by Simmons and Hoskins (1978) and Chang and Orlanski (1993). The mechanism for the initiation of the storm track is similar to the mechanism identified by Bischoff and Thompson (2014).

6. Discussion and conclusions

a. Summary

In this paper, we have discussed oceanic storm tracks: localized regions of anomalously high eddy kinetic energy. In the Southern Ocean, storm tracks are found in regions downstream of where Antarctic Circumpolar Current jets interact with large topographic features (WWH07). This phenomenon and its importance in mediating the zonally asymmetric meridional exchange of tracers in the Southern Ocean (Thompson and Sallée 2012) have motivated a series of idealized numerical experiments using parameters representative of the Southern Ocean and idealized, isolated topography to shed light on the physical mechanisms that control the onset, downstream development, and eventual termination of oceanic storm tracks, as well as to determine the influence of topographic shape on storm-track formation.

Each of our numerical experiments forms a storm track downstream of the topography that dissipates slowly downstream. We find that varying the height of the topography has little effect on either the storm-track intensity (as measured by integrated EKE) or the storm-track length. Varying the zonal length scale of the topography has a weak effect on the storm- track length but no clear influence on the storm-track magnitude. In all numerical experiments, a stationary meander that has the characteristics of a stationary Rossby wave is generated downstream of the topography. There is a moderate spatial scale separation between the standing meanders and transient eddies, the former having a wavelength of ~550 km (consistent with the scales expected from the Rossby wave dispersion relation) and the latter having a length scale of ~190 km, approximately equal to $2\pi R_{d_1}$. This result is in contrast to the atmospheric case where there is no clear scale separation between the stationary and transient disturbances (Kaspi and Schneider 2013).

The dynamics of the storm tracks are investigated using the wave activity flux of Takaya and Nakamura (2001) that enables the diagnosis of the relative contributions of eddy heat flux and ageostrophic fluxes of

Montgomery potential in a manner that is not dependent on the choice of averaging operator. The vertical wave activity flux shows eddy mass fluxes, and hence baroclinic instability, in the region immediately downstream of the topography. The spatial distribution of these fluxes is correlated with stationary wave phase lines, leading us to conclude that the region of enhanced baroclinic energy conversion is "forced" by the time-mean flow and occurs upstream of the peak storm-track EKE. Downstream of the maximum EKE, the horizontal wave activity flux becomes organized in the zonal direction, indicating that the downstream maintenance of the storm track is carried out by eddy-induced ageostrophic zonal transfers of Montgomery potential, similar to the situation described in Chang and Orlanski (1993).

Using these results, we propose a physical mechanism for the formation of storm tracks in the Southern Ocean, shown schematically in Fig. 9. The interaction of the Antarctic Circumpolar Current jets with large topographic features in the Southern Ocean leads to the formation of stationary meanders (Hughes 2005). The finite-amplitude perturbations to the mean flow caused by these waves modify the ocean environment to be locally baroclinically unstable, enabling the growth of strong, nonlinear transient eddies, a result consistent with Bischoff and Thompson (2014) and Abernathey and Cessi (2014). Eddies born in the growth regime disperse EKE downstream by ageostrophic Montgomery potential fluxes. As this energy propagates into the downstream development regime, new eddies grow, maintaining the storm track. This process is similar to the mechanisms described by Simmons and Hoskins (1979) and Chang and Orlanski (1993) and provides a simple conceptual framework for understanding the formation and persistence of storm tracks in the ocean. With this conceptual framework, the apparent insensitivity of the storm track to the shape of the topography is to be expected, as the shape of the storm track is governed by eddy–eddy interactions that take place downstream of the topography and the initiation region.

Our mechanism posits that the downstream development of oceanic storm tracks occurs because of the downstream dispersion of EKE due to ageostrophic Montgomery potential fluxes. In contrast to the commonly assumed mechanism (described in WWH07) of individual eddies forming in the regions of high baroclinicity and then propagating downstream into the regions of low baroclinicity, our mechanism posits that both the growth and decay of eddies occurs in the low baroclinicity regions, which, if true, would have implications for the parameterization of eddy tracer flux. Unlike in the midlatitude atmosphere (Danielson et al.

2006) and the subtropical oceans (O'Kane et al. 2014), the propagation of coherent eddies does not significantly contribute to the downstream development of the storm track.

In contrast to the study of atmospheric storm tracks by Kaspi and Schneider (2011, 2013), we find that the shape of oceanic storm tracks in our idealized model does not depend on the amplitude of the standing meander, which varies with the changing topographic length scale. In fact, while the growth regime would not exist without the presence of the standing meander, the "extension regime" exists well downstream of the standing meander's influence. It is unclear why this difference in behavior is observed, but it is likely that the scale separation between standing meander and transient eddies plays a role.

b. Implications and further work

As alluded to in Simmons and Hoskins (1979), the fact that large-scale flow features, such as the stationary meanders discussed in this article, are the primary origin of oceanic storm tracks has implications for their prediction and parameterization in coarse resolution models that are unable to completely resolve the transient eddies themselves. Although the length scales of the transient eddies are generally too small to be resolved by numerical simulations designed for long time scale investigations (such as the CMIP ensemble of GCMs), topographically induced stationary waves have sufficiently large length scales to be resolved by coarse-resolution models. The work undertaken here represents an important first step toward using the larger-scale stationary waves to parameterize the zonally asymmetric EKE fields. For example, if tracer flux is primarily downgradient in the growth regime and upgradient in the "downstream development regime" (WWH07), one could conceivably design a parameterization scheme using knowledge of the bulk parameters and the standing meanders.

Future work will concentrate on analysis of the growth of eddies in the downstream extension of the storm tracks to determine how the energy flux affects their growth rate and an analysis of their statistical properties for use in future parameterizations.

APPENDIX

Derivation of the Wave Activity Conservation Law in Isopycnal Coordinates

The linearized PV equation on a β plane is given by

$$\frac{\partial q'}{\partial t} + \langle \mathbf{u} \rangle_t \cdot \nabla_H q' + u' \cdot \nabla_H \langle q \rangle_t = \text{Forcing} - \text{Dissipation},$$

$$(\text{A1})$$

where the quasigeostrophic PV in isopycnal coordinates is (Berrisford et al. 1993)

$$q = \nabla_H^2 \psi + \beta y - \left(\frac{f_0^2 \rho_0}{g_0 \sigma_0} \right) \frac{\partial^2}{\partial \rho^2} \psi. \qquad (\text{A2})$$

To form an evolution equation for total perturbation energy e, we multiply Eq. (A1) by $-\psi$, as in Pedlosky (1987), while to form the equation for the time evolution of perturbation enstrophy $\mathcal{A}$, Eq. (A1) is multiplied by $q'/2|\nabla\langle q \rangle_t|$. Noting that the wave activity M is proportional to $[e/(\langle |\mathbf{u}| \rangle_t - c_p)] + \mathcal{A}$, the resulting QG perturbation energy and enstrophy equations are added together. Assuming WKBJ-like conditions, where the mean flow components vary more slowly in x and y than the perturbation components, we follow the manipulations of Takaya and Nakamura (2001) and move the constant term σ_0 outside the ∇ operator to give Eqs. (3) and (5).

REFERENCES

Abernathey, R., and P. Cessi, 2014: Topographic enhancement of eddy efficiency in baroclinic equilibration. *J. Phys. Oceanogr.,* **44,** 2107–2126, doi:10.1175/JPO-D-14-0014.1.

Adcroft, A., R. Hallberg, and M. Harrison, 2008: A finite volume discretization of the pressure gradient force using analytic integration. *Ocean Modell.,* **22,** 106–113, doi:10.1016/j.ocemod.2008.02.001.

Aiki, H., and T. Yamagata, 2006: Energetics of the layer-thickness form drag based on an integral identity. *Ocean Sci.,* **2,** 161–171, doi:10.5194/os-2-161-2006.

——, and K. J. Richards, 2008: Energetics of the global ocean: The role of layer-thickness form drag. *J. Phys. Oceanogr.,* **38,** 1845–1869, doi:10.1175/2008JPO3820.1.

Barnes, E. A., and D. L. Hartmann, 2012: The global distribution of atmospheric eddy length scales. *J. Climate,* **25,** 3409–3416, doi:10.1175/JCLI-D-11-00331.1.

Berrisford, P., J. C. Marshall, and A. A. White, 1993: Quasigeostrophic potential vorticity in isentropic coordinates. *J. Atmos. Sci.,* **50,** 778–782, doi:10.1175/1520-0469(1993)050<0778:QPVIIC>2.0.CO;2.

Bischoff, T., and A. F. Thompson, 2014: Configuration of a Southern Ocean storm track. *J. Phys. Oceanogr.,* **44,** 3072–3078, doi:10.1175/JPO-D-14-0062.1.

Blackmon, M. L., 1976: A climatological spectral study of the 500 mb geopotential height of the Northern Hemisphere. *J. Atmos. Sci.,* **33,** 1607–1623, doi:10.1175/1520-0469(1976)033<1607:ACSSOT>2.0.CO;2.

Bleck, R., 1985: On the conversion between mean and eddy components of potential and kinetic energy in isentropic and isopycnic coordinates. *Dyn. Atmos. Oceans,* **9,** 17–37, doi:10.1016/0377-0265(85)90014-4.

Bühler, O., 2014: A gentle stroll through EP flux theory. *Eur. J. Mech. B/Fluids,* **47,** 12–15, doi:10.1016/j.euromechflu.2014.01.010.

Chang, E. K. M., and I. Orlanski, 1993: On the dynamics of a storm track. *J. Atmos. Sci.,* **50,** 999–1015, doi:10.1175/1520-0469(1993)050<0999:OTDOAS>2.0.CO;2.

——, S. Lee, and K. L. Swanson, 2002: Storm track dynamics. *J. Climate,* **15,** 2163–2183, doi:10.1175/1520-0442(2002)015<02163:STD>2.0.CO;2.

Chapman, C. C., 2014: Southern Ocean jets and how to find them: Improving and comparing common jet detection methods. *J. Geophys. Res. Oceans,* **119,** 4318–4339, doi:10.1002/2014JC009810.

Chelton, D. B., R. A. deSzoeke, M. G. Schlax, K. El Naggar, and N. Siwertz, 1998: Geographical variability of the first baroclinic Rossby radius of deformation. *J. Phys. Oceanogr.,* **28,** 433–460, doi:10.1175/1520-0485(1998)028<0433:GVOTFB>2.0.CO;2.

——, M. G. Schlax, and R. M. Samelson, 2011: Global observations of nonlinear mesoscale eddies. *Prog. Oceanogr.,* **91,** 167–216, doi:10.1016/j.pocean.2011.01.002.

Danielson, R. E., J. R. Gyakum, and D. N. Straub, 2006: A case study of downstream baroclinic development over the North Pacific Ocean. Part II: Diagnoses of eddy energy and wave activity. *Mon. Wea. Rev.,* **134,** 1549–1567, doi:10.1175/MWR3173.1.

Farge, M., 1992: Wavelet transforms and their applications to turbulence. *Annu. Rev. Fluid Mech.,* **24,** 395–458, doi:10.1146/annurev.fl.24.010192.002143.

Gent, P. R., and J. C. McWilliams, 1990: Isopycnal mixing in ocean circulation models. *J. Phys. Oceanogr.,* **20,** 150–155, doi:10.1175/1520-0485(1990)020<0150:IMIOCM>2.0.CO;2.

Grotjahn, R., 2003: Baroclinic instability. *Encyclopedia of Atmospheric Sciences,* J. R. Holton, J. A. Curry, and J. A. Pyle, Eds., Academic Press, 179–188, doi:10.1016/B0-12-227090-8/00076-2.

Hallberg, R., and P. Rhines, 1996: Buoyancy-driven circulation in an ocean basin with isopycnals intersecting the sloping boundary. *J. Phys. Oceanogr.,* **26,** 913–940, doi:10.1175/1520-0485(1996)026<0913:BDCIAO>2.0.CO;2.

——, and A. Adcroft, 2009: Reconciling estimates of the free surface height in Lagrangian vertical coordinate ocean models with mode-split time stepping. *Ocean Modell.,* **29,** 15–26, doi:10.1016/j.ocemod.2009.02.008.

Hartmann, D. L., 1983: Barotropic instability of the polar night jet stream. *J. Atmos. Sci.,* **40,** 817–835, doi:10.1175/1520-0469(1983)040<0817:BIOTPN>2.0.CO;2.

Held, I. M., 1983: Stationary and quasi-stationary eddies in the extratropical troposphere: Theory. *Large-Scale Dynamical Processes in the Atmosphere,* B. Hoskins and R. Pearce, Eds., Academic Press, 127–168.

Hoskins, B. J., and P. J. Valdes, 1990: On the existence of storm-tracks. *J. Atmos. Sci.,* **47,** 1854–1864, doi:10.1175/1520-0469(1990)047<1854:OTEOST>2.0.CO;2.

——, and K. I. Hodges, 2002: New perspectives on the Northern Hemisphere winter storm tracks. *J. Atmos. Sci.,* **59,** 1041–1061, doi:10.1175/1520-0469(2002)059<1041:NPOTNH>2.0.CO;2.

——, and ——, 2005: A new perspective on Southern Hemisphere storm tracks. *J. Climate,* **18,** 4108–4129, doi:10.1175/JCLI3570.1.

Hughes, C. W., 1995: Rossby waves in the Southern Ocean: A comparison of TOPEX/POSEIDON altimetry with model predictions. *J. Geophys. Res.,* **100,** 15 933–15 950, doi:10.1029/95JC01380.

——, 2005: Nonlinear vorticity balance of the Antarctic Circumpolar Current. *J. Geophys. Res.,* **110,** C11008, doi:10.1029/2004JC002753.

——, and E. R. Ash, 2001: Eddy forcing of the mean flow in the Southern Ocean. *J. Geophys. Res.,* **106,** 2713–2722, doi:10.1029/2000JC900332.

Hughes, G. O., A. M. C. Hogg, and R. W. Griffiths, 2009: Available potential energy and irreversible mixing in the meridional overturning circulation. *J. Phys. Oceanogr.,* **39,** 3130–3146, doi:10.1175/2009JPO4162.1.

Jayne, S. R., and J. Marotzke, 2002: The oceanic eddy heat transport. *J. Phys. Oceanogr.,* **32,** 3328–3345, doi:10.1175/1520-0485(2002)032<3328:TOEHT>2.0.CO;2.

Kaspi, Y., and T. Schneider, 2011: Downstream self-destruction of storm tracks. *J. Atmos. Sci.,* **68,** 2459–2464, doi:10.1175/JAS-D-10-05002.1.

——, and ——, 2013: The role of stationary eddies in shaping midlatitude storm tracks. *J. Atmos. Sci.,* **70,** 2596–2613, doi:10.1175/JAS-D-12-082.1.

Klocker, A., and R. Abernathey, 2014: Global patterns of mesoscale eddy properties and diffusivities. *J. Phys. Oceanogr.,* **44,** 1030–1046, doi:10.1175/JPO-D-13-0159.1.

Lee, T., and P. Cornillon, 1996: Propagation and growth of Gulf Stream meanders between 75° and 45°W. *J. Phys. Oceanogr.,* **26,** 225–241, doi:10.1175/1520-0485(1996)026<0225:PAGOGS>2.0.CO;2.

Lee, W.-J., and M. Mak, 1996: The role of orography in the dynamics of storm tracks. *J. Atmos. Sci.,* **53,** 1737–1750, doi:10.1175/1520-0469(1996)053<1737:TROOIT>2.0.CO;2.

Lindzen, R. S., and B. Farrell, 1980: A simple approximate result for the maximum growth rate of baroclinic instabilities. *J. Atmos. Sci.,* **37,** 1648–1654, doi:10.1175/1520-0469(1980)037<1648:ASARFT>2.0.CO;2.

Masumoto, Y., and Coauthors, 2004: A fifty-year eddy-resolving simulation of the world ocean. *J. Earth Simul.,* **1,** 35–56. [Available online at www.jamstec.go.jp/esc/publication/journal/jes_vol.1/pdf/JES1-3.2-masumoto.pdf.]

Meredith, M. P., and A. M. Hogg, 2006: Circumpolar response of Southern Ocean eddy activity to a change in the southern annular mode. *Geophys. Res. Lett.,* **33,** L16608, doi:10.1029/2006GL026499.

Morrow, R., R. Coleman, J. Church, and D. Chelton, 1994: Surface eddy momentum flux and velocity variances in the Southern Ocean from Geosat altimetry. *J. Phys. Oceanogr.,* **24,** 2050–2071, doi:10.1175/1520-0485(1994)024<2050:SEMFAV>2.0.CO;2.

——, M. L. Ward, A. M. Hogg, and S. Pasquet, 2010: Eddy response to Southern Ocean climate modes. *J. Geophys. Res.,* **115,** C10030, doi:10.1029/2009JC005894.

Naveira Garabato, A. C., R. Ferrari, and K. L. Polzin, 2011: Eddy stirring in the Southern Ocean. *J. Geophys. Res.,* **116,** C09019, doi:10.1029/2010JC006818.

O'Kane, T. J., R. J. Matear, M. A. Chamberlain, E. C. J. Oliver, and N. J. Holbrook, 2014: Storm tracks in the Southern Hemisphere subtropical oceans. *J. Geophys. Res. Oceans,* **119,** 6078–6100, doi:10.1002/2014JC009990.

Orlanski, I., and J. Katzfey, 1991: The life cycle of a cyclone wave in the Southern Hemisphere. Part I: Eddy energy budget. *J. Atmos. Sci.,* **48,** 1972–1998, doi:10.1175/1520-0469(1991)048<1972:TLCOAC>2.0.CO;2.

——, and E. K. M. Chang, 1993: Ageostrophic geopotential fluxes in downstream and upstream development of baroclinic waves. *J. Atmos. Sci.,* **50,** 212–225, doi:10.1175/1520-0469(1993)050<0212:AGFIDA>2.0.CO;2.

——, and J. P. Sheldon, 1995: Stages in the energetics of baroclinic systems. *Tellus,* **47A,** 605–628, doi:10.1034/j.1600-0870.1995.00108.x.

Pedlosky, J., 1987: *Geophysical Fluid Dynamics.* 2nd ed. Springer-Verlag, 710 pp.

Plumb, R. A., 1983: A new look at the energy cycle. *J. Atmos. Sci.,* **40,** 1669–1688, doi:10.1175/1520-0469(1983)040<1669:ANLATE>2.0.CO;2.

——, 1985: On the three-dimensional propagation of stationary waves. *J. Atmos. Sci.,* **42,** 217–229, doi:10.1175/1520-0469(1985)042<0217:OTTDPO>2.0.CO;2.

Robinson, A. R., and J. C. McWilliams, 1974: The baroclinic instability of the open ocean. *J. Phys. Oceanogr.,* **4,** 281–294, doi:10.1175/1520-0485(1974)004<0281:TBIOTO>2.0.CO;2.

Sallée, J. B., K. Speer, R. Morrow, and R. Lumpkin, 2008: An estimate of Lagrangian eddy statistics and diffusion in the mixed layer of the Southern Ocean. *J. Mar. Res.,* **66,** 441–463, doi:10.1357/002224008787157458.

Shuckburgh, E., H. Jones, J. Marshall, and C. Hill, 2009: Understanding the regional variability of eddy diffusivity in the Pacific sector of the Southern Ocean. *J. Phys. Oceanogr.,* **39,** 2011–2023, doi:10.1175/2009JPO4115.1.

Simmons, A. J., and B. J. Hoskins, 1978: The life cycles of some nonlinear baroclinic waves. *J. Atmos. Sci.,* **35,** 414–432, doi:10.1175/1520-0469(1978)035<0414:TLCOSN>2.0.CO;2.

——, and ——, 1979: The downstream and upstream development of unstable baroclinic waves. *J. Atmos. Sci.,* **36,** 1239–1254, doi:10.1175/1520-0469(1979)036<1239:TDAUDO>2.0.CO;2.

Smith, S., 2003: *Digital Signal Processing: A Practical Guide for Engineers and Scientists.* Newnes, 650 pp.

Sokolov, S., and S. R. Rintoul, 2007: Multiple jets of the Antarctic Circumpolar Current south of Australia. *J. Phys. Oceanogr.,* **37,** 1394–1412, doi:10.1175/JPO3111.1.

Son, S.-W., M. Ting, and L. M. Polvani, 2009: The effect of topography on storm-track intensity in a relatively simple general circulation model. *J. Atmos. Sci.,* **66,** 393–411, doi:10.1175/2008JAS2742.1.

Takaya, K., and H. Nakamura, 2001: A formulation of a phase-independent wave-activity flux for stationary and migratory quasigeostrophic eddies on a zonally varying basic flow. *J. Atmos. Sci.,* **58,** 608–627, doi:10.1175/1520-0469(2001)058<0608:AFOAPI>2.0.CO;2.

Thompson, A. F., and J.-B. Sallée, 2012: Jets and topography: Jet transitions and the impact on transport in the Antarctic Circumpolar Current. *J. Phys. Oceanogr.,* **42,** 956–972, doi:10.1175/JPO-D-11-0135.1.

——, and A. C. Naveira Garabato, 2014: Equilibration of the Antarctic Circumpolar Current by standing meanders. *J. Phys. Oceanogr.,* **44,** 1811–1828, doi:10.1175/JPO-D-13-0163.1.

Venaille, A., G. K. Vallis, and K. S. Smith, 2011: Baroclinic turbulence in the ocean: Analysis with primitive equation and

quasigeostrophic simulations. *J. Phys. Oceanogr.,* **41,** 1605–1623, doi:10.1175/JPO-D-10-05021.1.

Ward, M. L., and A. M. Hogg, 2011: Establishment of momentum balance by form stress in a wind-driven channel. *Ocean Modell.,* **40,** 133–146, doi:10.1016/j.ocemod.2011.08.004.

Williams, R. G., C. Wilson, and C. W. Hughes, 2007: Ocean and atmosphere storm tracks: The role of eddy vorticity forcing. *J. Phys. Oceanogr.,* **37,** 2267–2289, doi:10.1175/JPO3120.1.

Wilson, C., B. Sinha, and R. G. Williams, 2009: The effect of ocean dynamics and orography on atmospheric storm tracks. *J. Climate,* **22,** 3689–3702, doi:10.1175/2009JCLI2651.1.

Witter, D. L., and D. B. Chelton, 1998: Eddy–mean flow interaction in zonal oceanic jet flow along zonal ridge topography. *J. Phys. Oceanogr.,* **28,** 2019–2039, doi:10.1175/1520-0485(1998)028<2019:EMFIIZ>2.0.CO;2.